Episodic stress and fluid pressure cycling in subducting oceanic crust during slow slip

E. Warren-Smith [1]*, B. Fry[1], L. Wallace[1,2], E. Chon[3], S. Henrys [1], A. Sheehan[3], K. Mochizuki [4], S. Schwartz[5], S. Webb[6] and S. Lebedev [7]

Slow slip events are part of a spectrum of aseismic processes that relieve tectonic stress on faults. Their spatial distribution in subduction zones has been linked to perturbations in fluid pressure within the megathrust shear zone and subducting oceanic crust. However, physical observations of temporal fluid pressure fluctuations through slow slip cycles remain elusive. Here, we use earthquake focal mechanisms recorded on an ocean-bottom seismic network to show that crustal stresses and fluid pressures within subducting oceanic crust evolve before and during slow slip events. Specifically, we observe that the retrieved stress ratio, which describes the relative magnitudes of the principal compressive stresses, systematically decreases before slow slip events in New Zealand's northern Hikurangi subduction zone, and subsequently increases during the evolution of each slow slip event. We propose that these changes represent the accumulation and release of fluid pressure within overpressured subducting oceanic crust, the episodicity of which may influence the timing of slow slip event occurrence on subduction megathrusts. This work contributes an improved understanding of the physical driving forces underlying slow subduction earthquakes, and a potential means by which to monitor stress and fluid pressure accumulation in such regions.

Recent seismic observations[1] and modelling[2] indicate that aseismic subduction interface slip during slow slip events[3] (SSEs) may be controlled by the presence of, and possible fluctuations in, near-lithostatic fluid pressure, P_f, within weak interface shear zones and subducting oceanic crust[4,5]. High P_f is inferred from a high ratio of seismic compressional and shear-wave velocities (V_p/V_s) and high Poisson's ratios on or near SSE-hosting subduction interfaces[4,6,7], indicating that an overpressured fluid reservoir is capped by a low permeability barrier[8]. Occasional breaching of this barrier, and its link to megathrust slip is commonly described by the 'fault-valve' model[8–11]. In this model, P_f varies temporally[9], peaking before fault slip, before coseismic fracture activation opens permeable pathways for fluid migration[10,11]. A subsequent P_f drop occurs until the system becomes resealed (for example, by hydrothermal precipitation[12–14]) and overpressure reaccumulates.

While the priming conditions[8] for subduction valving behaviour (for example, overpressure within conditionally permeable fault zones) have been observed globally[4–6], and evidence for post-megathrust rupture fluid drainage exists[10,11], temporal observations of precursory elevated P_f and subsequent decreases, particularly within the subducting slab where hydrothermal fluids are sourced, remain elusive. In situ effective stress measurements near the megathrust are restricted to shallow regions[15]. Hence, geophysical proxies are required to monitor temporal fluctuations in P_f at seismogenic depths. Here, we use relative principal stress magnitudes quantified by earthquake focal mechanism inversions as a proxy[16] for fluctuating P_f in New Zealand's northern Hikurangi subduction zone (Fig. 1) and identify changes in P_f within the downgoing slab correlated with SSE occurrence. This work expands previous temporally static, spatial snapshots of elevated P_f in SSE regions[1,4] into the temporal dimension, and offers constraints on the physical driving forces behind SSE recurrence intervals in subduction zones.

Pore pressure changes and the stress tensor

Fluid saturation within subducting oceanic crust is formed by de-watering reactions[17] and downwards fluid pumping into tensional fractures[18]. Fluctuations in this P_f act to alter the effective normal stress, σ_n', on fractures (where $\sigma_n' = \sigma_n - P_f$). An increase in P_f reduces σ_n' and broadens the orientation of faults that satisfy the reactivation criteria; a wider range of fault orientations become susceptible to slip (Fig. 2b). When σ_1 is subvertical, high P_f promotes instability of subvertical dipping strike–slip faults in addition to normal faults dipping at ~60°[16].

Fluctuating P_f can therefore be quantified by examining diversity in active fault orientations and estimating the stress (or shape) ratio, $R = (\sigma_1 - \sigma_2)/(\sigma_1 - \sigma_3)$ (or effective stress ratio, R', in the presence of fluid pressure), through earthquake focal mechanism inversion. The R value retrieved this way (hereafter, R_{retr}) has been shown to correlate negatively with varying P_f during geothermal injection in transtensional regions with low overall R ($R < 0.6$)[16]. This negative correlation exists because the broader fault plane distribution accompanying high P_f modifies how well sampled the fault orientations are, which influences R_{retr}[16] but may not represent true variability in R'.

The negative correlation between R_{retr} and P_f may also have a physical origin. In an isotropic medium with round pores, P_f acts the same in all directions; changing P_f produces no change in the relative magnitudes of the three principal compressive effective stresses, σ_1', σ_2' and σ_3'. However, the response to changing P_f in a medium with axial, planar cracks produces different poroelastic effects on the three principal effective stresses, depending on the fracture orientations[19]. Within subducting oceanic crust, bending-related, fluid-filled fractures[18,20] control the large-scale anisotropy[21]. These fractures strike margin-parallel with their poles in the σ_1/σ_3 plane (Fig. 2a). In this instance, increasing P_f produces a larger poroelastic response in σ_1' and σ_3' than in σ_2' (Fig. 2b), reducing the
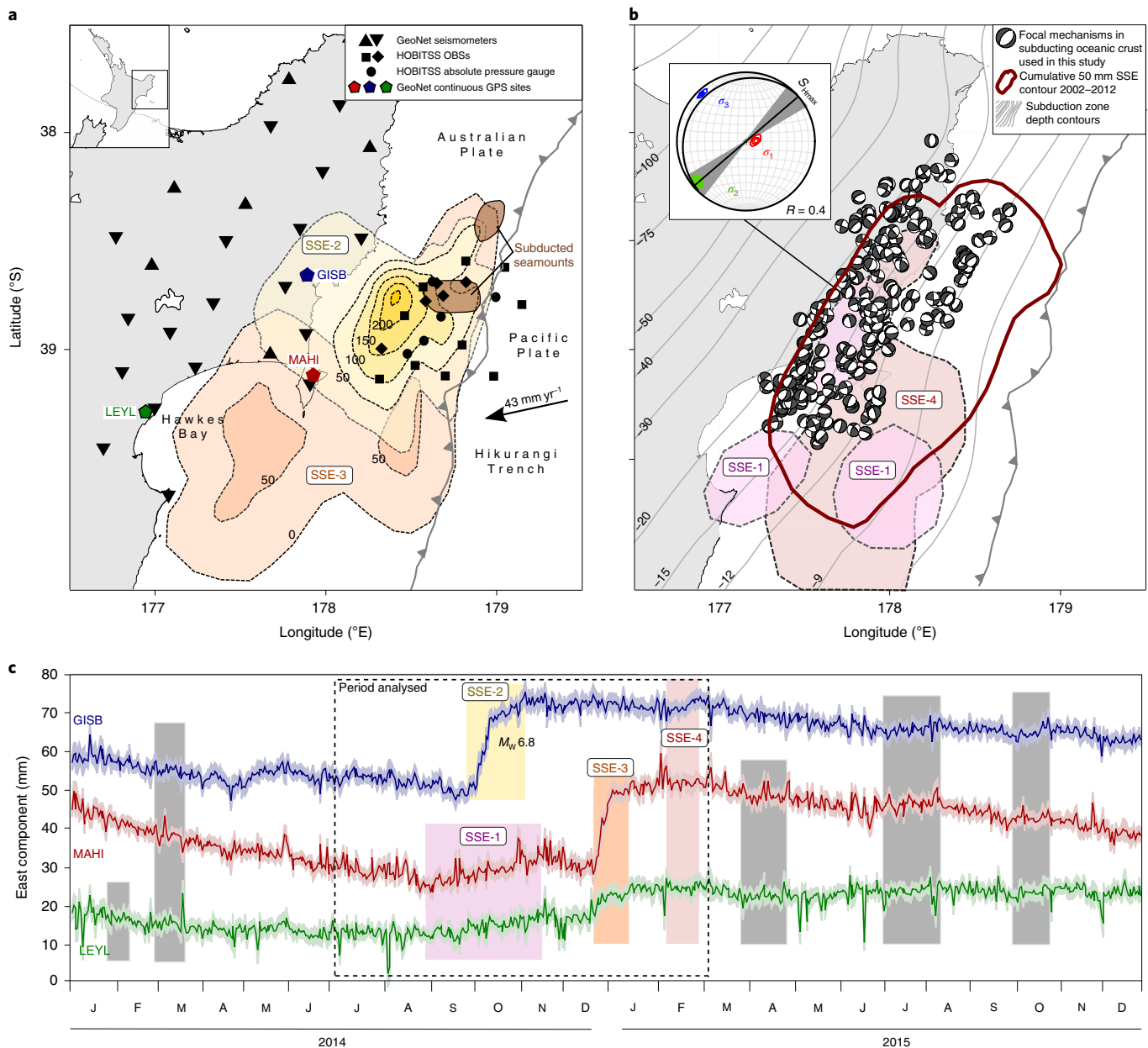
Fig. 1 | Overview of northern Hikurangi, and the seismic and geodetic networks, SSEs and seismicity utilized in this study. a, Shaded contours (in mm) show geodetic slip models for two large SSEs. **b**, Lower-plate focal mechanisms used for stress analysis. Shaded contours (in mm) show geodetic slip models of two smaller transients. The thick red contour shows cumulative 50 mm SSE slip distribution between 2002 and 2012[22]. Inset, triaxial stress field orientation (lower hemisphere) for the mechanisms shown in the main panel. Contours show 90% uncertainties. The black great circle shows the subduction zone orientation. **c**, Geodetic signals (green, blue and red lines) and timings of SSEs (shaded boxes, coloured are those analysed here). Additional GPS time series and SSE model fits are included in Supplementary Figs. 1 and 2.

R' value[19]. In this instance, R_{retr} may more closely mirror physical changes in R'. Fluctuations in R_{retr} within the crust in SSE regions may therefore provide a proxy for relative changes in P_f and a test for the fault-valve model.

Stress tensor changes during SSEs

The northern Hikurangi subduction zone hosts large, shallow 2–3-week-long SSEs every 1–2 years[22]. In addition, smaller transient events can occur up to several times a year (Fig. 1). In 2014–2015, an ocean-bottom seismic and geodetic network—the Hikurangi Ocean Bottom Investigation of Tremor and Slow Slip (HOBITSS)—recorded four SSEs with a range of durations, magnitudes and spatial extents (Fig. 1 and Supplementary Table 1). In August 2014, a small, 2.5-month-long SSE (SSE-1) was followed by a spatially distinct, but temporally overlapping M_w 6.8 SSE in September 2014 (SSE-2) near Gisborne that involved interface slip close to the trench[23]. A third (SSE-3) and fourth event (SSE-4) followed in December 2014 and February 2015, respectively (Fig. 1).

We calculated focal mechanisms for earthquakes ($M_w > 1.8$) in the national GeoNet seismicity catalogue (see Methods) over a time period covering all four SSEs, using HOBITSS and onshore GeoNet seismic stations (Fig. 1b). Few earthquakes occur on the subduction interface. Instead, we focused on 278 events that occurred within the subducting Pacific oceanic crust, which hosts the majority of
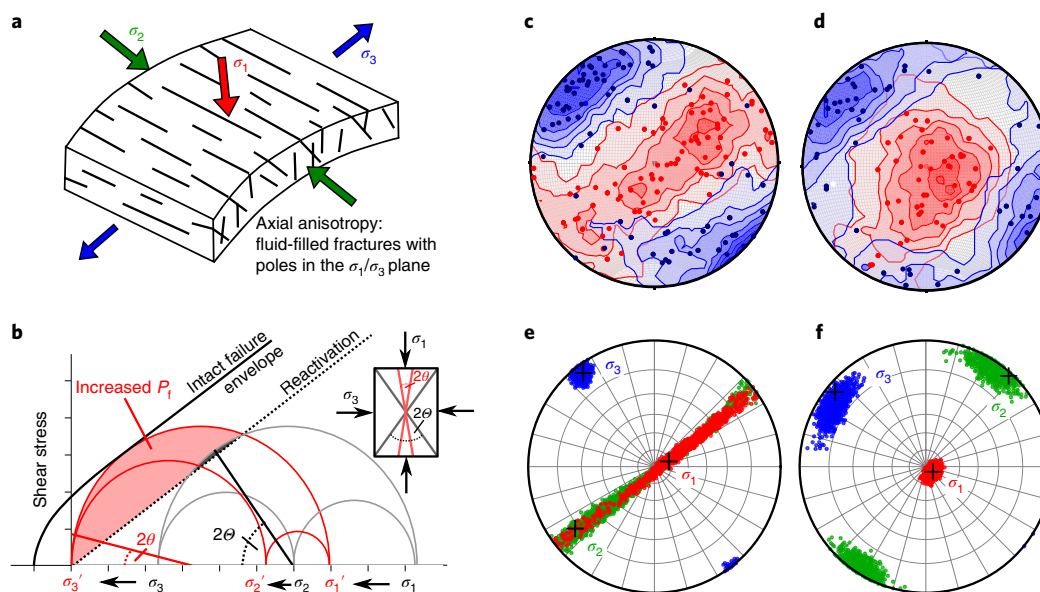
Fig. 2 | Links between intraslab faulting and P_f changes. a, Schematic of tensional, bending-related fractures in subducting oceanic crust. **b**, Mohr diagram showing the effect of increasing P_f (red Mohr circle) in fractures within an anisotropic medium such as that shown in **a**[19]. Grey and red shaded regions show the orientations of faults that are active under different P_f states. Steeply dipping faults at $\theta°$ to σ_1 are only reactivated alongside high P_f. **c,d**, Orientations of the P (red) and T (blue) axes of focal mechanisms at the initiation (**c**; $n=140$) and shutdown (**d**; $n=80$) of all SSEs. **e,f**, Triaxial stress field orientations at the initiation (**e**) and shutdown (**f**) of SSE periods.

subduction zone seismicity in the region. These events define a 13–15-km-thick zone of intraslab seismicity, consistent with the thickness of the incoming Hikurangi Plateau[24].

Earthquakes in the northern Hikurangi slab exhibit both normal slip on margin-parallel-striking faults and strike–slip events orientated with margin-parallel pressure axes (P axes; Fig. 1b). Inversion for the triaxial stress field (see Methods) reveals that σ_1 is subvertical and σ_3 is orientated margin-perpendicular, guided by tensional slab pull (Fig. 1b, inset). σ_2 trends margin-parallel and corresponds to the maximum horizontal compressive stress direction (S_{Hmax}). The background value for R_{retr} calculated using all focal mechanisms is 0.42 ± 0.24.

To quantify temporal changes in the stress tensor, we grouped our focal mechanisms into moving windows of 20 events overlapping by 15 events, chosen to minimize smoothing and retain temporal resolution (Supplementary Fig. 5). We performed damped (to discriminate robust, temporal variations in stress that are strongly required by the model) and undamped stress inversions[25,26] for each window. Because the accuracy of R_{retr} depends on ambiguity in the earthquake nodal plane, we implemented a fault instability algorithm[27] to identify the nodal plane (see Methods) before each inversion[16]. We present the results assuming that the algorithm selects the correct plane both 100% ($F=1.0$) and 50% ($F=0.5$) of the time (Fig. 3).

R_{retr} varies by ~0.6 over the time period, with consistent minima in R_{retr} of ~0.25 occurring before, or overlapping with, the onset of all four documented SSEs (Fig. 3b and Supplementary Fig. 6), independent of fault plane ambiguity. The minimum at the start of SSE-1 is only visible in the undamped inversion result, as it was brief and was lost as noise during damping. During each SSE, a 3–4-week increase to $R_{retr} > 0.5$ is observed, before a subsequent decrease in R_{retr} begins at the end of each SSE, reaching a minimum R_{retr} value of ~0.25 at the start of the next SSE.

To test whether R_{retr} changes are spatially linked to a particular SSE, we analysed the focal mechanisms occurring beneath and immediately (within 10 km) down-dip from SSE-2 (Fig. 3c) and

SSE-3 (Fig. 3d). Both subsets show longer-duration decreases (over a few months) in R_{retr} than in Fig. 3b, suggesting that the margin-wide analysis is influenced by diachronous changes in R_{retr} across multiple interacting slow slip cycles. Both subsets still show a minimum R_{retr} of ~0.25 before SSE initiation, importantly suggesting that a threshold is reached within the footprint of the subsequent SSE. Additionally, the increase in R_{retr} during and following each event is smaller than in Fig. 3b, suggesting that the SSE-induced changes in R_{retr} do not exclusively occur within the SSE footprint.

Furthermore, during low R_{retr} periods before SSEs, P axes plunge both steeply and shallowly (trending margin-parallel), while tension axes (T axes) trend margin-perpendicular only, indicating a mix of both normal and strike–slip faulting (Fig. 2c). During high R_{retr} periods following SSEs, P axes only plunge steeply, indicating purely normal faulting (Fig. 2d). This change is apparent in the triaxial stress field inversions as well. During low R_{retr} periods, overlap between the σ_1 and σ_2 axes (Fig. 2e) indicates that they are close in magnitude (Supplementary Fig. 7). Following SSEs, the principal axes are distinct and well defined as a normal faulting regime (Fig. 2f).

Physical mechanism for the stress tensor changes

Stress tensor changes have previously been seismologically observed following subduction zone earthquakes[28]. One way that these changes occur is through displacement of shear stress acting on the subduction interface by coseismic and postseismic slip. If the change in shear stress, or stress drop, $\Delta\tau$, is large compared with the effective differential stress ($\sigma_1' - \sigma_3'$), a rotation in the stress field following rupture is anticipated, succeeded by a return to prerupture orientations as τ is reaccumulated, typically over months to years[28]. This process is illustrated by the 2011 M_w 9.0 Tohoku-Oki (Japan) subduction earthquake, where a 20° rotation in the σ_1 plunge was observed[29], reflecting the high stress drop ($\Delta\tau = $~20 MPa) of the mainshock[30].

An additional process that may change the retrieved stress tensor is a static change in imposed stress on receiver faults, quantified by
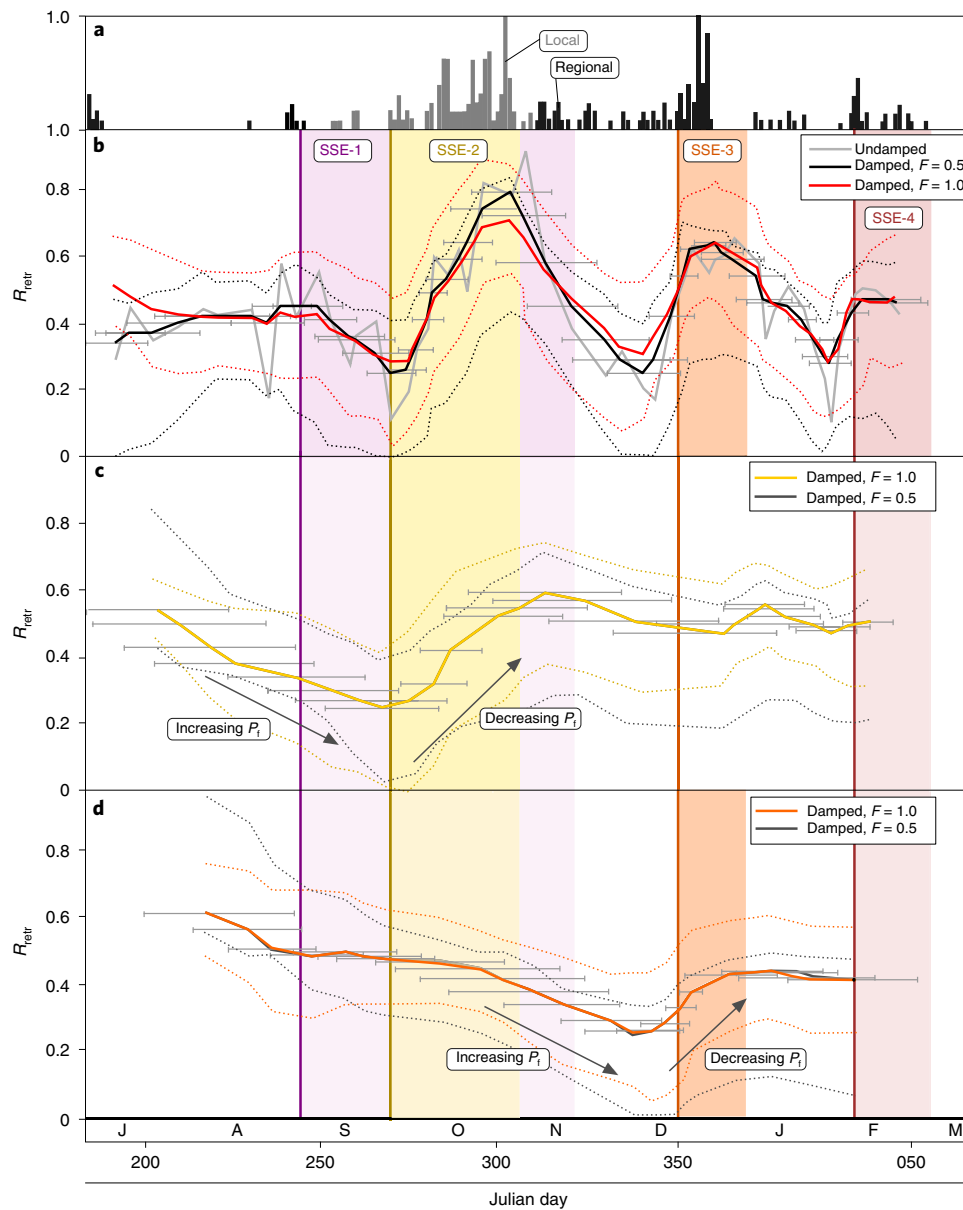
Fig. 3 | Observed stress tensor changes during northern Hikurangi SSEs. a, Normalized daily northern Hikurangi tremor detections showing local[41] and regional catalogues[42]. **b**, Temporal variation in R_{retr} within subducting oceanic crust, calculated using a damped (black and red) and undamped (grey) inversion approach[25] ($n=278$). Black and red lines show $F=0.5$ and $F=1.0$ probability of correct nodal plane selection, respectively. Vertical errors (dashed lines) indicate 95% confidence intervals. Horizontal errors show the time period of events used to calculate each R_{retr} value. SSE timings are coloured and labelled to match those in Fig. 1. **c,d**, Same as in **b**, but for subsets of events occurring beneath and immediately down-dip from SSE-2 (**c**; $n=153$; yellow) and SSE-3 (**d**; $n=139$; orange).

the Coulomb failure stress (CFS), where $CFS=\tau-\mu\sigma_n'$, and μ is the friction coefficient[31]. The dependence of CFS changes on receiver fault orientation means that some faults will be brought closer to failure, while others may be brought further away, thus changing the active faulting distribution and the retrieved stress tensor. For example, fewer intra-SSE strike–slip earthquakes could be explained by decreasing CFS on these extensional faults by down-dip oriented compression within the slab from interface slip (Supplementary Fig. 8).

However, these processes cannot fully explain our observations. First, SSE stress drops are typically orders of magnitude lower ($\Delta\tau=\sim10$–300 kPa)[32] than for fast subduction earthquakes. Any observable stress tensor changes are therefore unlikely to be produced by interface shear stress displacements, even if the

interface is assumed to be 'weak' ($\sigma_1'-\sigma_3'\leq20$ MPa), as required to explain stress orientations[33] and gravitational force balances[34]. Second, CFS models for SSE-2 indicate that both strike–slip and normal fault activity become unfavourable within the slab during and following interface slip (Supplementary Fig. 8), yet normal faults remain active throughout each SSE. Furthermore, neither process can explain the rapid return to increasing focal mechanism orientation diversity (Supplementary Fig. 7b) following interface slip shutdown.

Instead, we propose that our observations represent transient fluctuations in P_f within fault zones in the subducting oceanic crust (Fig. 4), which migrate (down a pressure gradient) into the overlying interface, creating an increase in P_f sufficient to trigger slow slip[2].
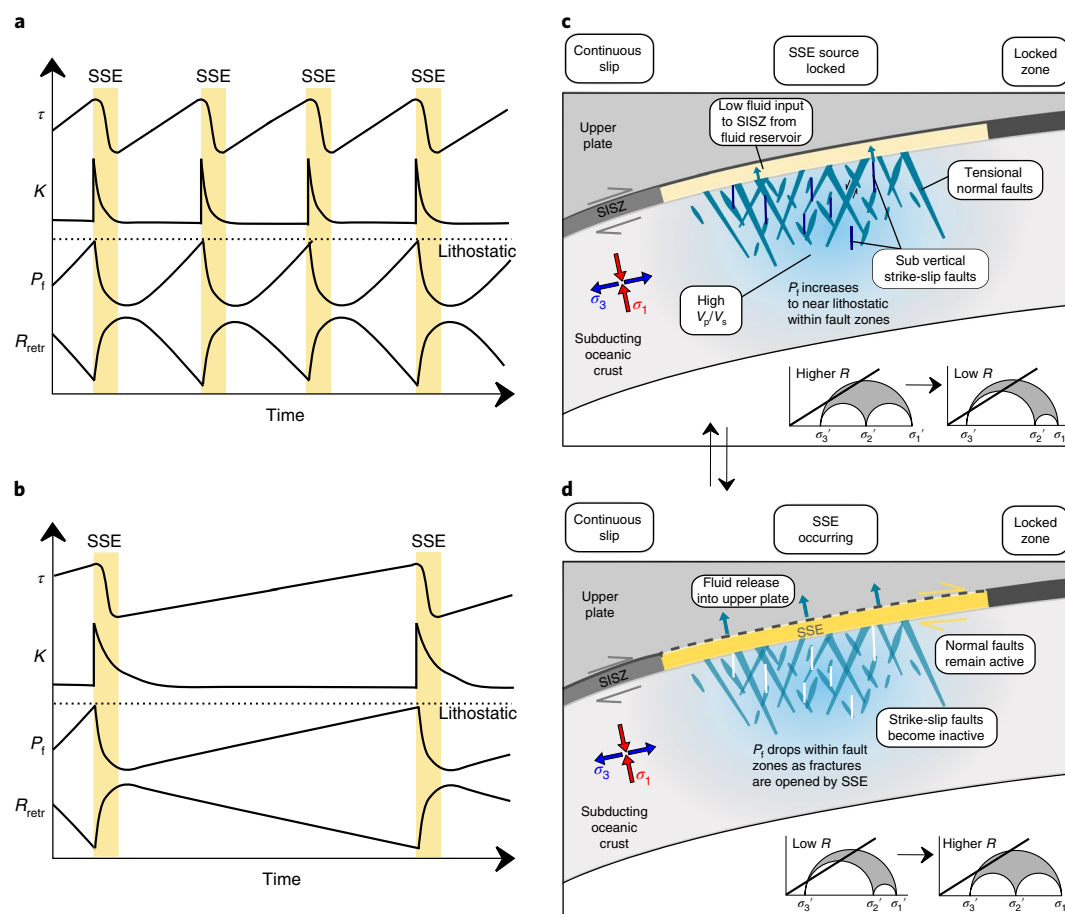
Fig. 4 | Physical model of fluid accumulation and release, and the effect on the stress tensor. a,b, Periodic variability in key physical parameters across the margin (**a**) and for an individual source area (**b**)[9]. Changes in P_f and R_{retr} appear faster for the whole margin because of multiple, interfering SSE cycles. P_f accumulates beneath a particular SSE slip zone over several months. **c**, Inter-SSE period. SISZ, subduction interface shear zone. **d**, Intra-SSE period. See text for a full description. Schematics in **c** and **d** are not to scale.

P_f decreases within individual intraslab faults are anticipated to occur relatively quickly. During interface slip in SSEs, strain-induced fracture opening[35] produces a concomitant drop in P_f as fast crack propagation exceeds the fluid advection rate into the new volume from the groundmass[12]. P_f may also decrease as enhanced permeability allows drainage from intraslab faults into the subduction plate boundary and overriding plate[9–11,36]. This P_f drop is observed seismologically as decreasing strike–slip activity and an increase in R_{retr}[16].

Subsequent, slower increases in P_f are then anticipated as slab fractures and the subduction interface become resealed by precipitate-hosting fluid advection and diffusion[12–14,37], and permeability is reduced. This sealing is geologically inferred to occur over a few weeks[12] to several months[37] and is therefore compatible with the episodicity we observe seismologically in R_{retr} and inferred P_f. As P_f increases to near-lithostatic values, reduced σ_n' means subvertical faults become favourably orientated and seismically active, which is observed as a decrease in R_{retr}.

The consistent minima in $R_{retr} \sim 0.25$ (Fig. 3b) implies that a maximum P_f threshold may be reached, which triggers SSE initiation. First, P_f changes within the lower fluid reservoir may locally increase P_f within the subduction plate boundary through hydro-fracturing-enhanced vertical permeability. Assuming fluid pressure is lost during upwards migration along the negative pressure gradient, any P_f increase within the subduction plate boundary will be smaller than that experienced within the slab, yet remains

sufficient to lower effective normal stress, triggering slip[2]. Alternatively, increasing P_f in the interface-bounding slab may reduce the system's elastic loading stiffness, K, below the critical stiffness K_c required for slip[38] according to:

$$K < K_c = -(a-b)\sigma_n'/D_c$$

where D_c is a critical slip distance over which fault strength evolves and $(a-b)$ is the friction rate parameter, which is required to be negative for slip instability nucleation.

This model is supported by our analysed earthquakes' locations within a region of elevated $V_p/V_s > 1.8$ (ref. [39]), indicating that they occur within relatively fluid-rich rocks beneath the down-dip extent of repeated SSEs (Supplementary Fig. 9). Mantle-derived helium isotope signatures at hot springs along the east coast also suggest a deep, oceanic crust-derived flux of fluid surfacing near Mahia Peninsula, above a section of the interface that slipped in all four SSEs[40]. Furthermore, tremor activity[41,42] is highest during R_{retr} increases (Fig. 3a), suggesting that fluid redistribution occurs near the interface at these times.

Assuming the slab is in down-dip tension and experiencing both extensional and shear failure, $4T < (\sigma_1' - \sigma_3') < 5.66T$, where T is the tensional strength for intact basalt ($T = \sim 14\,\mathrm{MPa}$[43]). Hence, differential stress cannot be higher than 55–80 MPa. An observed change in R' of 0.5 (half of $\sigma_1' - \sigma_3'$) could therefore represent roughly a 40 MPa change in P_f. Importantly, R_{retr} is affected by

noise in mechanism orientations and background R; regions with lower overall R and higher data noise exhibit larger variability in R_{retr} given the same change in P_f as for a region with low data noise and high background R[16]. This effect precludes quantification of absolute changes in P_f represented by our observed R_{retr} fluctuations. Synthetic testing[16] indicates that it is still likely to be several MPa given a background R value of ~0.4. While rapid P_f changes of this magnitude are unlikely to reflect changes in de-watering reaction rates, localized opening (to near-hydrostatic gradients) and sealing (to near-lithostatic gradients) of fluid compartments within slab fracture networks may produce several MPa changes in pore pressure[44,45], and can be sufficient to explain the magnitude of our observed changes. This way, the time scales for repeated P_f accumulation may be controlled by feedback between hydrothermal mineral precipitation in the interface shear zone and tensional slab fault zones[13,14], and fracture opening related to SSE-induced crustal strain[35].

Concluding implications for slow slip

The recent discovery of aseismic displacements on subduction megathrusts during SSEs has complicated the simple model of stress loading and release during the earthquake cycle. Quantifying how stress on and around the megathrust is accumulated and released during SSE cycles is crucial for understanding basic subduction system physics and accurately forecasting earthquake and tsunami hazards in areas where SSEs occur[46]. To date, research has focused on stress changes following SSEs, and their causal effect on subsequent major earthquakes[46–49]. However, we present evidence that the distribution and timing of SSEs may be in response to external, episodically imposed stress changes that can vary both spatially and temporally, and hence explain the wide variety in SSE occurrence rates observed globally. Furthermore, our observations highlight the need for an improved understanding of frictional variability in terms of P_f redistribution in order to fully physically model SSE behaviour[50]. Finally, we postulate that increased monitoring of stress ratio changes in subduction zones may offer a means of improving forecasts of slow and possibly even fast subduction slip.

Online content

Any methods, additional references, Nature Research reporting summaries, source data, statements of code and data availability and associated accession codes are available at https://doi.org/10.1038/s41561-019-0367-x.

References

1. Kodaira, S. et al. High pore fluid pressure may cause silent slip in the Nankai Trough. *Science* **304**, 1295–1298 (2004).
2. Liu, Y. & Rice, J. R. Spontaneous and triggered aseismic deformation transients in a subduction fault model. *J. Geophys. Res. Solid Earth* **112**, B09404 (2007).
3. Dragert, H., Wang, K. & James, T. S. A silent slip event on the deeper Cascadia subduction interface. *Science* **292**, 1525–1528 (2001).
4. Audet, P., Bostock, M. G., Christensen, N. I. & Peacock, S. M. Seismic evidence for overpressed subducted oceanic crust and megathrust fault sealing. *Nature* **457**, 76–78 (2009).
5. Kato, A. et al. Variations of fluid pressure within the subducting oceanic crust and slow earthquakes. *Geophys. Res. Lett.* **37**, L14310 (2010).
6. Christensen, N. I. Pore pressure and oceanic crustal seismic structure. *Geophys. J. R. Astron. Soc.* **79**, 411–423 (1984).
7. Sibson, R. H. & Rowland, J. V. Stress, fluid pressure and structural permeability in seismogenic crust, North Island, New Zealand. *Geophys. J. Int.* **154**, 584–594 (2003).
8. Sibson, R. H. Conditions for fault-valve behaviour. *Geol. Soc. Lond. Spec. Publ.* **54**, 15–28 (1990).
9. Sibson, R. H. Stress switching in subduction forearcs: implications for overpressure containment and strength cycling on megathrusts. *Tectonophysics* **600**, 142–152 (2013).
10. Husen, S. & Kissling, E. Postseismic fluid flow after the large subduction earthquake of Antofagasta, Chile. *Geology* **29**, 847–850 (2001).
11. Nakajima, J. & Uchida, N. Repeated drainage from megathrusts during episodic slow slip. *Nat. Geosci.* **11**, 351–356 (2018).
12. Fisher, D. M. & Brantley, S. L. The role of silica redistribution in the evolution of slip instabilities along subduction interfaces: constraints from the Kodiak accretionary complex, Alaska. *J. Struct. Geol.* **69**, 395–414 (2014).
13. Audet, P. & Bürgmann, R. Possible control of subduction zone slow-earthquake periodicity by silica enrichment. *Nature* **510**, 389–392 (2014).
14. Saishu, H., Okamoto, A. & Otsubo, M. Silica precipitation potentially controls earthquake recurrence in seismogenic zones. *Sci. Rep.* **7**, 13337 (2017).
15. Kitajima, H. & Saffer, D. M. Elevated pore pressure and anomalously low stress in regions of low frequency earthquakes along the Nankai Trough subduction megathrust. *Geophys. Res. Lett.* **39**, L23301 (2012).
16. Martínez-Garzón, P., Vavryčuk, V., Kwiatek, G. & Bohnhoff, M. Sensitivity of stress inversion of focal mechanisms to pore pressure changes. *Geophys. Res. Lett.* **43**, 8441–8450 (2016).
17. Peacock, S. A. Fluid processes in subduction zones. *Science* **248**, 329–337 (1990).
18. Faccenda, M., Gerya, T. V. & Burlini, L. Deep slab hydration induced by bending-related variations in tectonic pressure. *Nat. Geosci.* **2**, 790–793 (2009).
19. Healy, D. Anisotropic poroelasticity and the response of faulted rock to changes in pore-fluid pressure. *Geol. Soc. Lond. Spec. Publ.* **367**, 201–214 (2012).
20. Ranero, C. R., Morgan, J. P., McIntosh, K. & Reichert, C. Bending-related faulting and mantle serpentinization at the Middle America trench. *Nature* **425**, 367–373 (2003).
21. Faccenda, M., Burlini, L., Gerya, T. V. & Mainprice, D. Fault-induced seismic anisotropy by hydration in subducting oceanic plates. *Nature* **455**, 1097–1100 (2008).
22. Wallace, L. M. & Beavan, J. Diverse slow slip behavior at the Hikurangi subduction margin, New Zealand. *J. Geophys. Res. Solid Earth* **115**, B12402 (2010).
23. Wallace, L. M. et al. Slow slip near the trench at the Hikurangi subduction zone, New Zealand. *Science* **352**, 701–704 (2016).
24. Mochizuki, K. et al. Wide-angle OBS velocity structure and gravity modeling along the SAHKE transect, southern North Island, New Zealand. In *Proc. 11th SEGJ International Symposium* 527–529 (Society of Exploration Geophysicists of Japan, 2013).
25. Hardebeck, J. L. & Michael, A. J. Damped regional-scale stress inversions: methodology and examples for southern California and the Coalinga aftershock sequence. *J. Geophys. Res. Solid Earth* **111**, B11310 (2006).
26. Martínez-Garzón, P., Kwiatek, G., Ickrath, M. & Bohnhoff, M. MSATSI: a MATLAB package for stress inversion combining solid classic methodology, a new simplified user-handling, and a visualization tool. *Seismol. Res. Lett.* **85**, 896–904 (2014).
27. Vavryčuk, V. Iterative joint inversion for stress and fault orientations from focal mechanisms. *Geophys. J. Int.* **199**, 69–77 (2014).
28. Hardebeck, J. L. & Okada, T. Temporal stress changes caused by earthquakes: a review. *J. Geophys. Res. Solid Earth* **123**, 1350–1365 (2018).
29. Hasegawa, A. et al. Change in stress field after the 2011 great Tohoku-Oki earthquake. *Earth Planet. Sci. Lett.* **355**, 231–243 (2012).
30. Hasegawa, A., Yoshida, K. & Okada, T. Nearly complete stress drop in the 2011 M_w 9.0 off the Pacific coast of Tohoku Earthquake. *Earth Planets Space* **63**, 35 (2011).
31. King, G. C., Stein, R. S. & Lin, J. Static stress changes and the triggering of earthquakes. *Bull. Seismol. Soc. Am.* **84**, 935–953 (1994).
32. Brodsky, E. E. & Mori, J. Creep events slip less than ordinary earthquakes. *Geophys. Res. Lett.* **34**, L16309 (2007).
33. Hardebeck, J. L. Stress orientations in subduction zones and the strength of subduction megathrust faults. *Science* **349**, 1213–1216 (2015).
34. Lamb, S. Shear stresses on megathrusts: implications for mountain building behind subduction zones. *J. Geophys. Res. Solid Earth* **111**, B07401 (2006).
35. Rivet, D. et al. Seismic evidence of nonlinear crustal deformation during a large slow slip event in Mexico. *Geophys. Res. Lett.* **38**, L08308 (2011).
36. Magee, M. E. & Zoback, M. D. Evidence for a weak interplate thrust fault along the northern Japan subduction zone and implications for the mechanics of thrust faulting and fluid expulsion. *Geology* **21**, 809–812 (1993).
37. Taetz, S., John, T., Bröcker, M., Spandler, C. & Stracke, A. Fast intraslab fluid-flow events linked to pulses of high pore fluid pressure at the subducted plate interface. *Earth Planet. Sci. Lett.* **482**, 33–43 (2018).
38. Leeman, J. R., Saffer, D. M., Scuderi, M. M. & Marone, C. Laboratory observations of slow earthquakes and the spectrum of tectonic fault slip modes. *Nat. Commun.* **7**, 11104 (2016).
39. Eberhart-Phillips, D., Reyners, M., Bannister, S., Chadwick, M. & Ellis, S. Establishing a versatile 3-D seismic velocity model for New Zealand. *Seismol. Res. Lett.* **81**, 992–1000 (2010).

40. Giggenbach, W. F., Sano, Y. & Wakita, H. Isotopic composition of helium, and CO_2 and CH_4 contents in gases produced along the New Zealand part of a convergent plate boundary. *Geochim. Cosmochim. Acta* **57**, 3427–3455 (1993).
41. Todd, E. K. et al. Earthquakes and tremor linked to seamount subduction during shallow slow slip at the Hikurangi Margin, New Zealand. *J. Geophys. Res. Solid Earth* **123**, 6769–6783 (2018).
42. Todd, E. K. & Schwartz, S. Y. Tectonic tremor along the northern Hikurangi Margin, New Zealand, between 2010 and 2015. *J. Geophys. Res. Solid Earth* **121**, 8706–8719 (2016).
43. Schultz, R. A. Brittle strength of basaltic rock masses with applications to Venus. *J. Geophys. Res. Planets* **98**, 10883–10895 (1993).
44. Vrolijk, P. Tectonically driven fluid flow in the Kodiak accretionary complex, Alaska. *Geology* **15**, 466–469 (1987).
45. Byerlee, J. D. Model for episodic flow of high-pressure water in fault zones before earthquakes. *Geology* **21**, 303–306 (1993).
46. Kaneko, Y., Wallace, L. M., Hamling, I. J. & Gerstenberger, M. C. Simple physical model for the probability of a subduction-zone earthquake following slow slip events and earthquakes: application to the Hikurangi megathrust, New Zealand. *Geophys. Res. Lett.* **45**, 3932–3941 (2018).
47. Ruiz, S. et al. Intense foreshocks and a slow slip event preceded the 2014 Iquique M_w 8.1 earthquake. *Science* **345**, 1165–1169 (2014).
48. Ito, Y. et al. Episodic slow slip events in the Japan subduction zone before the 2011 Tohoku-Oki earthquake. *Tectonophysics* **600**, 14–26 (2013).
49. Mazzotti, S. & Adams, J. Variability of near-term probability for the next great earthquake on the Cascadia subduction zone. *Bull. Seismol. Soc. Am.* **94**, 1954–1959 (2004).
50. Cruz-Atienza, V. M., Villafuerte, C. & Bhat, H. S. Rapid tremor migration and pore-pressure waves in subduction zones. *Nat. Commun.* **9**, 2900 (2018).

Author contributions

E.W.-S. performed the data analysis, prepared the figures, interpreted the results and wrote the manuscript. B.F. designed the study, and contributed to interpretation and editing of the manuscript. L.W. performed geodetic inversions of SSEs, and contributed to data collection, and interpretation and editing of the manuscript. E.C. and A.S. contributed to focal mechanism calculation and editing of the manuscript. S.H., K.M., S.S., S.L. and S.W. contributed to data collection, and interpretation and editing of the manuscript.

Competing interests

The authors declare no competing interests.

Additional information

Supplementary information is available for this paper at https://doi.org/10.1038/s41561-019-0367-x.

Reprints and permissions information is available at www.nature.com/reprints.

Correspondence and requests for materials should be addressed to E.W.-S.

Publisher's note: Springer Nature remains neutral with regard to jurisdictional claims in published maps and institutional affiliations.

Methods

Geodetic SSE slip distribution inversion. SSE slip inversions were undertaken with TDEFNODE (http://www.web.pdx.edu/~mccaf/defnode/manual/tdefnode.html), which is a nonlinear, time-dependent inversion code that applies simulated annealing to downhill simplex minimization. Our approach to the TDEFNODE inversions in this study was identical to that used in previous north Hikurangi SSE studies[51]. All continuous Global Positioning System (GPS) data time series used in this study are available from www.geonet.org.nz. We inverted the continuous GPS time series of GeoNet sites at the northern and central Hikurangi margin for: (1) an initiation time and time constants describing the temporal evolution of four transient events at the northern and central Hikurangi margin during the study period; and (2) the maximum amplitude of slip at 40 nodes on the plate interface offshore from the central and northern Hikurangi margin for each transient. Slip on fault patches between the nodes was determined by bi-linear interpolation. TDEFNODE uses basis functions to describe the temporal evolution of slip at the nodes, thus reducing the number of free parameters required to replicate the temporal evolution of the SSE. We assumed a Gaussian function to approximate the time history of the SSEs. We also assumed that slip on the plate interface occurs in the direction of plate motion slip determined by previous elastic block modelling results[52]; for the east coast, slip is almost completely in the down-dip direction. Fits to many of the time series are shown in Supplementary Fig. 1, and slip models are shown in Supplementary Fig. 2.

Focal mechanism calculation. Earthquakes that occurred within the study region and time period were selected from the national GeoNet catalogue (www.geonet.org.nz), and phase (direct Pg and Sg) arrivals and Pg-wave polarities were manually picked on up to 46 land (GeoNet; broadband and short period) and HOBITSS Ocean Bottom Seismometer (OBS) stations[53]. Earthquakes were initially located in a one-dimensional velocity model[54] for the northern Hikurangi region using a linearized inversion algorithm (HYPOCENTER[55]). Distributions of polarities across the focal sphere were visually examined using FOCMEC[56] to identify which events held sufficient coverage for further analysis. Events with $M < 1.9$ were too small to allow for accurate analysis. Following this quality-control phase, earthquakes were relocated using NonLinLoc[57] within a three-dimensional velocity model[39], incorporating average velocity model uncertainties in travel times, and phase-pick timing errors. A Bayesian focal mechanism calculation method[58] was used to calculate the final fault plane solutions for events. This method incorporates velocity model and location uncertainties to calculate the probability density function for each take-off angle on the focal sphere. Larger uncertainty in location therefore leads to a larger scatter for each polarity point on the sphere, which is included in the mechanism calculation. Examples of mechanisms calculated this way are shown in Supplementary Fig. 3.

We extracted lower-plate events by examining their locations relative to the interface model of ref. [59] derived from earthquake relocations, and active source studies where available[60]. Depth uncertainties for focal mechanisms were small (<2 km) owing to good offshore and onshore station azimuthal coverage, allowing accurate identification of Pacific crust earthquakes versus interface or upper-plate events based on their location and mechanisms combined. Examples of the effect of changing hypocentral depth on focal mechanisms for select events are shown in Supplementary Fig. 4.

Stress ratio calculation. For our spatial stress inversion in the inset of Fig. 1b, we adopted the method from ref. [61], which calculates the triaxial stress field using focal mechanisms through a Bayesian approach and allows for inclusion of mechanism rotation errors arising from velocity model and polarity uncertainties. For our temporal stress inversions, we adopted the methods of refs. [25,62] within the MSATSI MATLAB package[26]. This method uses a damped inversion to remove stress rotation artefacts in noisy data, which may be present in an undamped moving-window series of inversions, and includes a bootstrap resampling approach to quantify confidence intervals of the stress parameters. This damped inversion approach uses a damping parameter (the relative weighting between the data misfit and model length in the minimization), which is chosen from a trade-off curve to produce a balance between excessive misfit and unnecessary model length. We performed a one-dimensional time-varying stress inversion on time windows of 20 events, overlapping by 15 events, within a single spatially constrained region.

We additionally implemented a fault instability algorithm[27] to identify the nodal plane before each inversion though a joint inversion for both stress and fault orientation. This approach does not influence the orientations of the principal axes derived from the stress inversion, but is required to accurately retrieve the stress, or shape ratio, R_{retr}, which is sensitive to the correct choice of nodal versus auxiliary planes. The algorithm calculates the instability constraint, I:

$$I = (\tau + \mu (\sigma_n + 1)) / (\mu + \sqrt{(1 + \mu^2)})$$

where μ is the coefficient of friction, and τ and σ_n are the normalized shear and normal tractions. I is calculated for both possible faults of the focal mechanism, and the nodal plane is chosen as the one that has the highest value of I (that is, is the most unstable in the acting stress field). μ is estimated by running the inversion with several values for friction, and adopting the value that produces the highest overall instability of faults.

Coulomb stress modelling. We calculated changes in CFS, $\sigma_f = \tau - \mu \sigma_n'$, where μ is the coefficient of friction, on receiver faults to examine the role of static interface offsets on changing the distribution of earthquake faulting styles during and following slow slip. We used the interface slip model for SSE-2 from ref. [23] within Coulomb software version 3.3 (ref. [63]) to calculate $\Delta \sigma_f$ on both potential fault planes of mechanisms consistent with the shallowest and steepest P axes orientations shown in Fig. 2c. These orientations included normal faults orientated with strike/dip/rake = 050/60/−90 and 230/60/−90, and strike–slip faults orientated with strike/dip/rake = 090/90/0 and 270/90/180. We observed a similar distribution of decreases and increases in $\Delta \sigma_f$ regardless of the coefficient of friction (0.1–1.0) used. We display our results in Supplementary Fig. 8 using a coefficient of friction of 0.4.

Data availability

Onshore GeoNet seismic waveforms were obtained from https://www.geonet.org.nz/data/types/seismic_waveforms. Offshore HOBITSS raw seismic and geodetic data are archived at the Incorporated Research Institutions for Seismology Data Management Center (https://doi.org/10.7914/SN/YH_2014).

Code availability

Code used for the geodetic slip inversions (TDEFNODE) is available from http://www.web.pdx.edu/~mccaf/defnode/manual/tdefnode.html. MATLAB code (MSATSI) used for temporal stress inversions is available from https://www.induced.pl/software/msatsi.

References

51. Wallace, L. M. et al. Large-scale dynamic triggering of shallow slow slip enhanced by overlying sedimentary wedge. *Nat. Geosci.* **10**, 765–770 (2017).
52. Wallace, L. M. et al. The kinematics of a transition from subduction to strike-slip: an example from the central New Zealand plate boundary. *J. Geophys. Res.* **117**, B02405 (2012).
53. Wallace, L., Sheehan, A., Schwartz, S. & Webb, S. *Hikurangi Ocean Bottom Investigation of Tremor and Slow Slip* (International Federation of Digital Seismograph Networks, 2014); https://doi.org/10.7914/SN/YH_2014
54. Reyners, M., Eberhart-Phillips, D. & Stuart, G. A three-dimensional image of shallow subduction: crustal structure of the Raukumara Peninsula, New Zealand. *Geophys. J. Int.* **137**, 873–890 (1999).
55. Lienert, B. R., Berg, E. & Frazer, L. N. HYPOCENTER: an earthquake location method using centered, scaled, and adaptively damped least squares. *Bull. Seismol. Soc. Am.* **76**, 771–783 (1986).
56. Snoke, J. A. FOCMEC: focal mechanism determinations. *Int. Handb. Earthquake Eng. Seismol.* **85**, 1629–1630 (2003).
57. Lomax, A. *The NonLinLoc Software Guide* (ALomax Scientific, 2008); http://alomax.free.fr/nlloc
58. Walsh, D., Arnold, R. & Townend, J. A Bayesian approach to determining and parametrizing earthquake focal mechanisms. *Geophys. J. Int.* **176**, 235–255 (2009).
59. Williams, C. A. et al. Revised interface geometry for the Hikurangi subduction zone, New Zealand. *Seismol. Res. Lett.* **84**, 1066–1073 (2013).
60. Bell, R. et al. Seismic reflection character of the Hikurangi subduction interface, New Zealand, in the region of repeated Gisborne slow slip events. *Geophys. J. Int.* **180**, 34–48 (2010).
61. Arnold, R. & Townend, J. A Bayesian approach to estimating tectonic stress from seismological data. *Geophys. J. Int.* **170**, 1336–1356 (2007).
62. Lund, B. & Townend, J. Calculating horizontal stress orientations with full or partial knowledge of the tectonic stress tensor. *Geophys. J. Int.* **170**, 1328–1335 (2007).
63. Toda, S., Stein, R. S., Sevilgen, V. & Lin, J. *Coulomb 3.3 Graphic-Rich Deformation and Stress-Change Software for Earthquake, Tectonic, and Volcano Research and Teaching—User Guide* No. 2011-1060 (US Geological Survey, 2011).